Supporting information

Ion-Channel-Mediated Gradient Acceptor Distribution for Hard Lead-free Piezoceramics

Yongqi Pan[1#], Xinya Feng[2#], Zhourui Zhang[1], Yi Ding[1], Fei Li[2], Shujun Zhang[3*], Ting Zheng[1*] and Jiagang Wu[1*]

1 College of Materials Science and Engineering, Sichuan University, Chengdu 610065, China.

2 Electronic Materials Research Laboratory, Key Laboratory of the Ministry of Education and State Key Laboratory for Mechanical Behavior of Materials, School of Electronic and Information Engineering, Xi'an Jiaotong University, Xi'an 710049, China.

3 Department of Chemistry, City University of Hong Kong, Kowloon, 999077, Hong Kong, China

Figure S1 (a) the X-ray diffraction patterns of KT compared with standard card; illustration shows the micro-morphological structure of KT; (b) the EPR spectrum of pure KT and (c) the structural diagram of KT

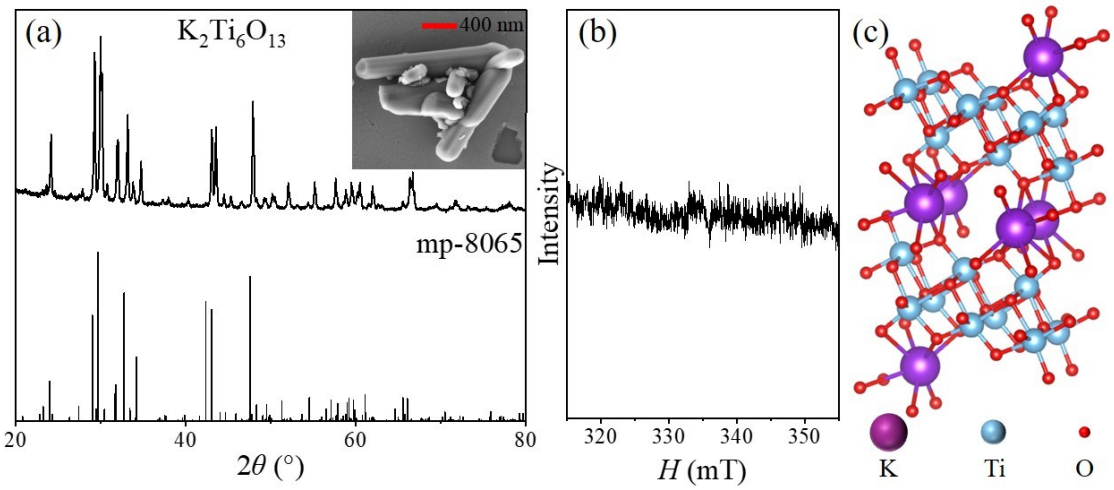

Figure S1 shows the structural and morphological characterizations of the synthesized $K_2Ti_6O_{13}$ (KT). As shown in Figure S1(a), the XRD patterns of synthetized KT generally matches the standard reference data, confirming the successful formation of the intended crystalline phase. The inset presents the SEM image of KT sample, exhibiting a characteristic long-strip morphology. Although minor agglomeration is observed, the functional mechanism relies on the interface between KT and KNN. As long as the KT surfaces are in contact with the KNN grains, they effectively facilitate Cu redistribution, making perfect rod isolation unnecessary for the intended gradient effect. And the EPR spectroscopy Figure S1(b) confirms that there are no obvious paramagnetic defect signals in pure KT such as reduced Ti^{3+} species or certain trapped-electron centers ($V_O^{\cdot\cdot}$). The KT phase features a tunnel structure consisting of edge- and corner-sharing TiO_6 octahedra. During high-temperature sintering in air, alkali metal oxides are susceptible to volatilization. This process typically follows a Schottky-like mechanism where the loss of potassium is charge-compensated by the formation of oxygen vacancies, described by the reaction:

$$O_O^{\times} + 2K_K^{\times} \rightarrow 2V_K^{'} + V_O^{\cdot\cdot} + K_2O(g)$$

In this configuration, the negative charge of the potassium vacancies ($V_K^{'}$) is balanced by the positive charge of $V_{\ddot{O}}$, rather than by the reduction of Ti^{4+} to paramagnetic Ti^{3+}. Consequently, all resulting defect species ($V_K^{'}$, $V_{\ddot{O}}$) and Ti^{4+} remain diamagnetic. This defect mechanism explains the presence of abundant vacancies essential for ion transport while remaining consistent with the absence of paramagnetic signals in the EPR spectrum. The abundant potassium vacancies within the tunnels are critical as they lower the energy barrier for ion migration, effectively acting as "ionic highways" that facilitate the rapid transport and redistribution of ions during the sintering process. Figure S1(c) provides a schematic illustration of the crystal structure of KT. The framework is composed of open TiO_6 octahedral aligned in a tunnel-like configuration, which is typical of Anderson-Wadsley-type alkali titanates.

Figure S2: the process of diffusion experiments

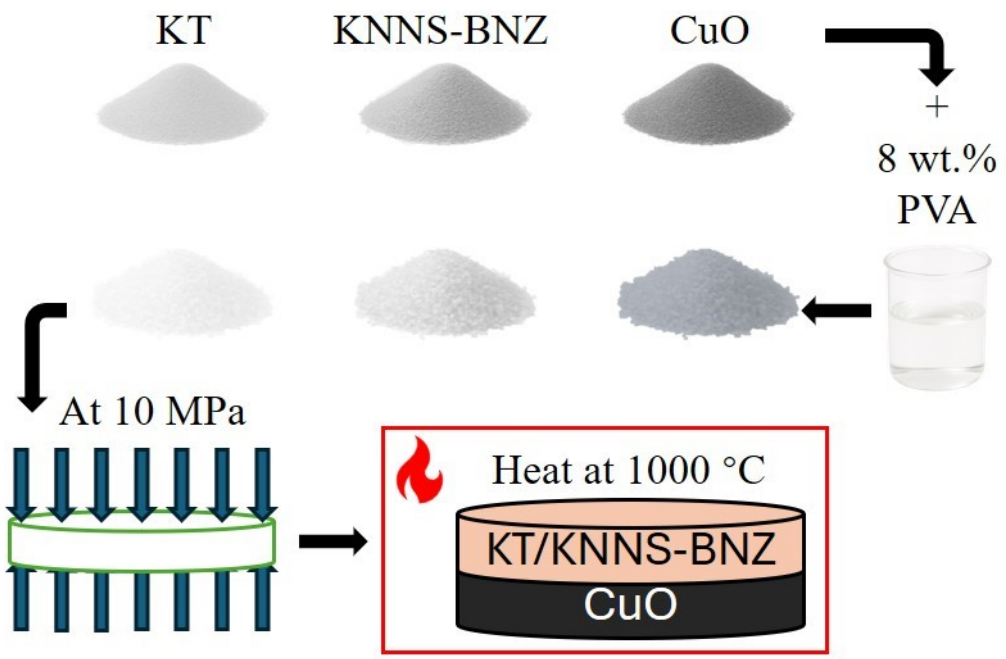

Figure S2 shows the process of diffusion experiments, KT and KNNS-BNZ powders were independently synthesized, ground, and mixed with 8 wt.% PVA solution as a binder, then uniaxially pressed into green pellets at 10 MPa. Separately, CuO powder was also pressed into green pellets under the same conditions. For each test, a KT (or KNNS-BNZ) pellet was stacked on top of a CuO pellet to form a bilayer diffusion couple, with CuO placed at the bottom to minimize gravitational effects on ion penetration. The stacked structures were sintered at 1000 °C for various durations, a temperature selected to prevent CuO melting while enabling sufficient Cu ion diffusion.

Figure S3: the ε_r and tan (δ) -T curves of (a) 0.5 wt.% and (b) 1 wt.% KT across temperature from -100 °C to 270 °C

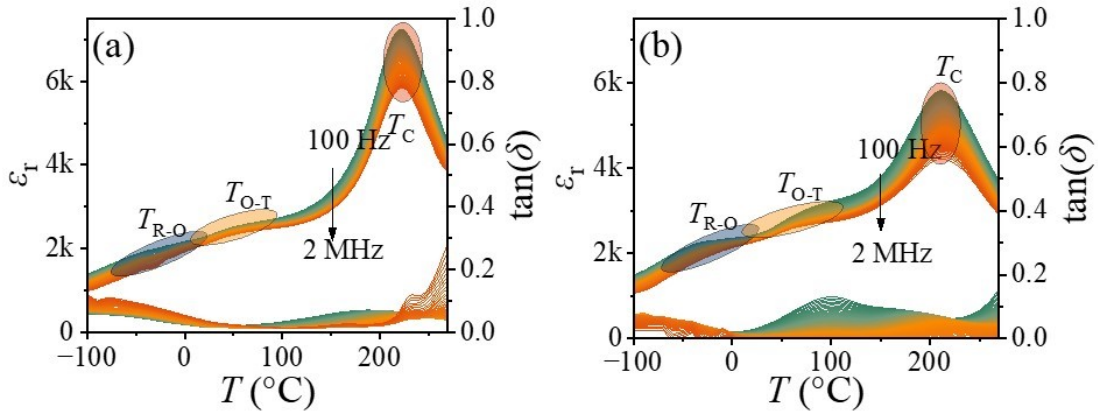

Figure S3(a) and (b) shows the ε_r -T curves of 0.5 wt.% and 1 wt.% KT measured under different frequencies, and the positions and shapes of all dielectric peaks of the two samples are basically the same. The corresponding dielectric loss curves are also shown in the figure, exhibiting a similar behavior to the permittivity. And the dielectric loss remains low throughout the entire measured temperature range, with tan δ consistently below 0.1, suggesting excellent dielectric stability and low energy dissipation in the KT-modified ceramics.

Figure S4: the dielectric constant and dielectric loss versus temperature at different frequencies for (c) 0 wt.% KT, (d) 0.5 wt.% KT, (e) 0.75 wt.% KT and (f) 1 wt.% KT, respectively

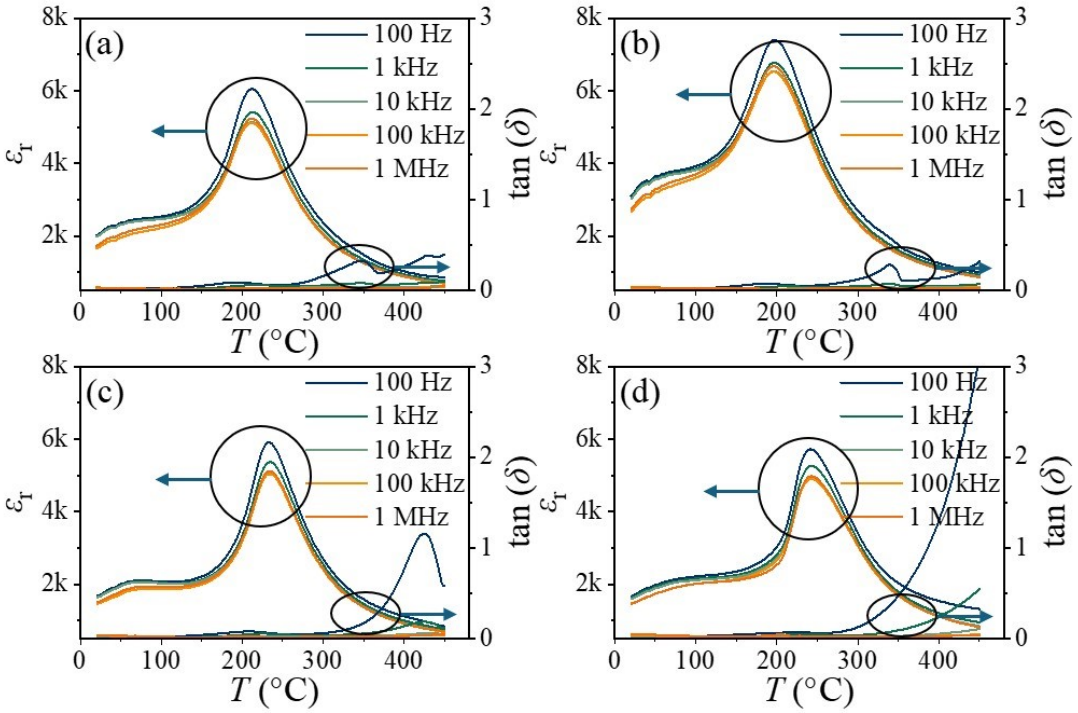

Figures S4(a-d) illustrate the variation of dielectric constant and dielectric loss with temperature for various samples measured at different frequencies. The dielectric temperature peak position remains nearly unchanged across all samples, indicating that KT has little impact on the phases transition points.

Figure S5: the X-ray diffraction pattern at room temperature.

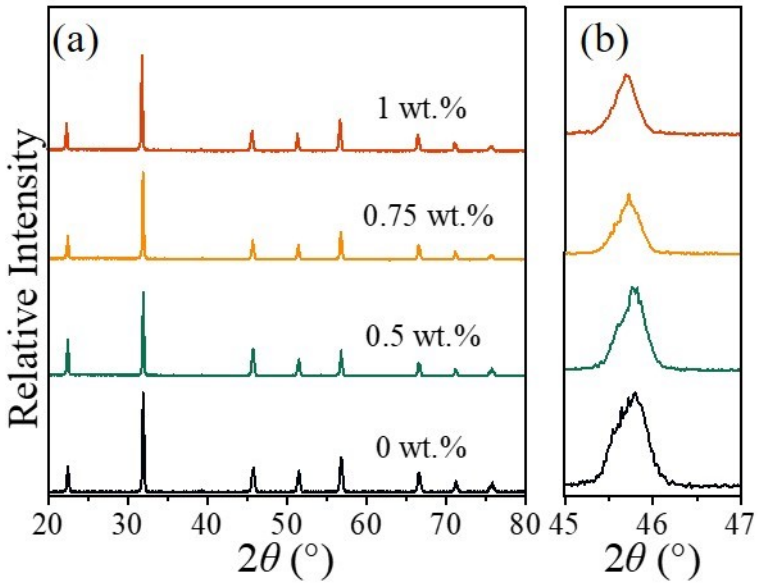

Figure S5(a) presents the X-ray diffraction patterns of various samples at 2θ = 20 °-80 °, To better assess any changes in phase structure, the (200) diffraction peaks are enlarged in Figure S5 (b), it is evident that with the increase of the KT content, neither the position nor the shape of the diffraction peaks undergoes significant changes, indicating that after doping KT, the primary phase structure of the KNN ceramics remains.

Figure S6: the XRD patterns fitted using Rietveld refinement using three-phase standard cards

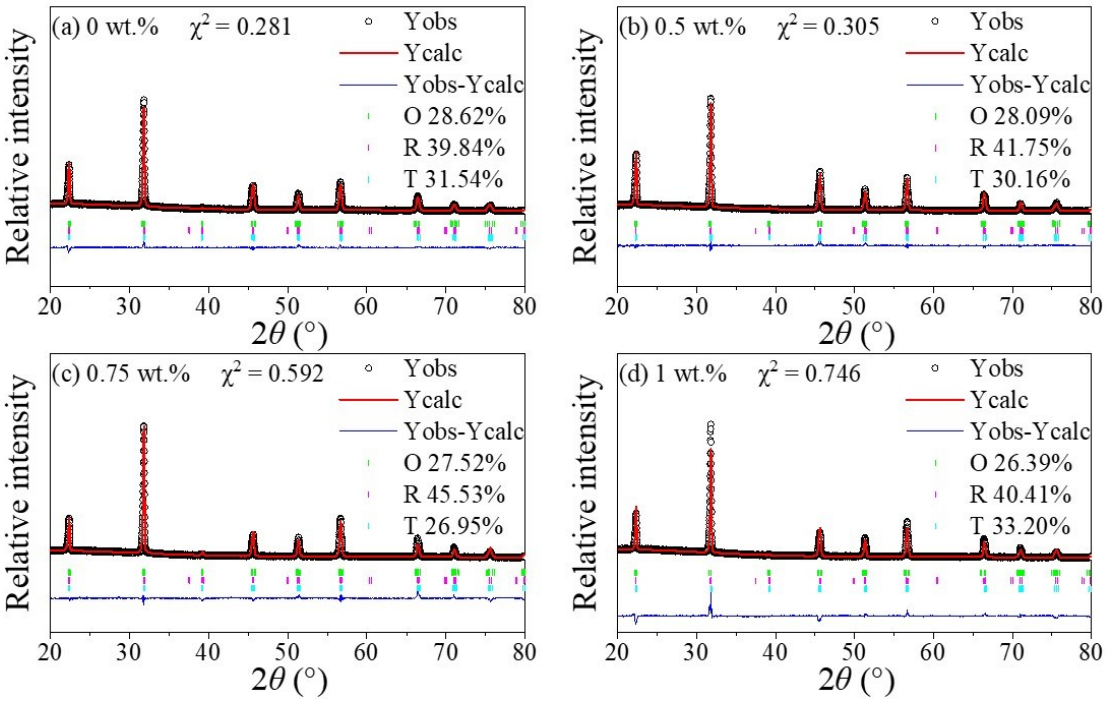

Figure S6 displays the refined XRD patterns of different samples, processed using Fullprof with three standard cards, and the ratio of these phases are given in the illustration, as can be seen, the fitted curves of all samples match the test results, and the phase ratios of the fitted samples did not change significantly, indicates that KT does not dissolve in the lattice to change the phase structure significantly.

Figure S7: the SEM images of (a) 0 wt.% KT, (b)0.5 wt.% KT, (c) 0.75 wt.% KT and (d) 1 wt.% KT

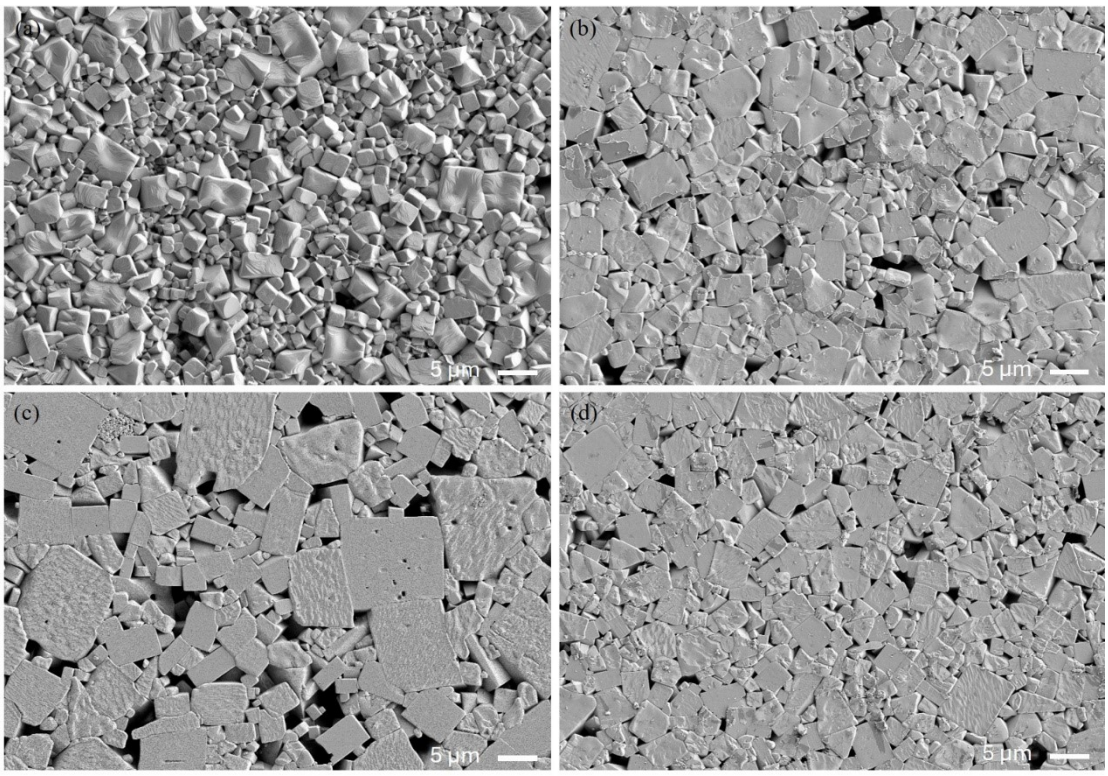

Figure S7 illustrates the SEM images, with the introduction of KT the grain size increases and then decreases, where the 0.75 wt.% KT has the largest grain size and shows two different grain sizes, which should be related to the KT-induced heterogeneous distribution of Cu ions, the increase in oxygen vacancies during sintering leads to an abnormal grain growth.

Figure S8: (a) XPS profiles of O1S for different samples, fitting results for (b) 0.5 wt.% KT, (c) 0.75 wt.% KT, (d) 1 wt.% KT

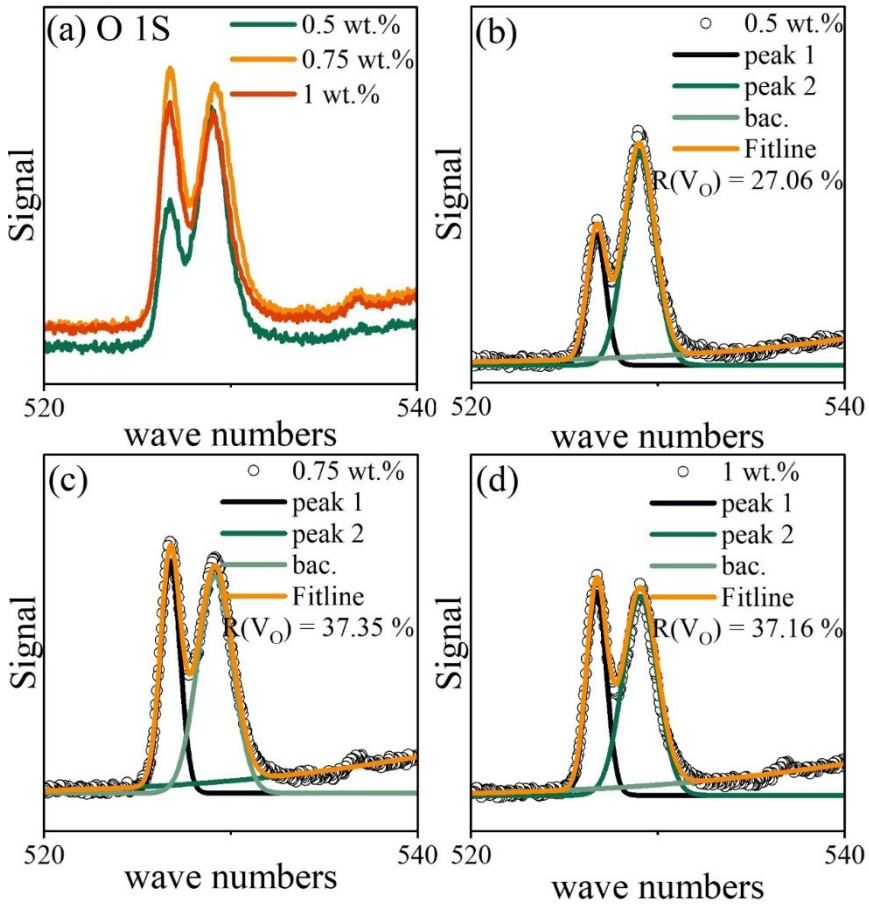

Figure S8 shows the X-ray photoelectron spectroscopy (XPS) O1S spectra of different samples, with each spectrum deconvoluted using Gaussian fitting. The O1s spectrum can be subdivided into lattice oxygen and oxygen vacancies, which have binding energies around 529 eV and 531 eV, respectively. The O vacancy concentration can be obtained by the ratio of peak area at 529 eV to the overall peak area. It can be seen that with the increase of KT, the vacancy concentration increases and then decreases, which is basically the same as the results of the EPR test. However, note that while XPS detects oxygen vacancies at the surface, EPR captures the overall defect distribution within the entire sample, leading to some differences in the absolute values.

Figure S9: (a) TEM image showing the grain morphology of the sample with 0.75 wt.% KT; the KT region is delineated by a white outline. (b-d) Elemental mapping of Cu, Ti, and O, respectively, corresponding to the region in (a), and the illustration in the image shows the element count intensity distribution curve corresponding to the white arrow, along with the result after FFT smoothing, confirming the presence and spatial distribution of KT. (e) Schematic illustration of the Cu ion gradient enrichment (the blue dashed region represents the Cu-enriched region containing KT, and the purple region indicates the Cu-depleted active region). To investigate the local structural influence of KT, HAADF images were obtained from regions near (f1) and far from (g1) the KT phase. The corresponding simulated ε_{yy} strain maps (f2, g2) indicate higher strain accumulation near the KT region. Further magnified HAADF images from subregions (f3, g3) were used to extract local bond lengths. The B-site bond length distributions (f4, g4) and A-site bond length distributions (f5, g5) reveal distinct differences between the two areas, demonstrating that the KT phase induces local lattice distortion and strain field modulation in its vicinity.

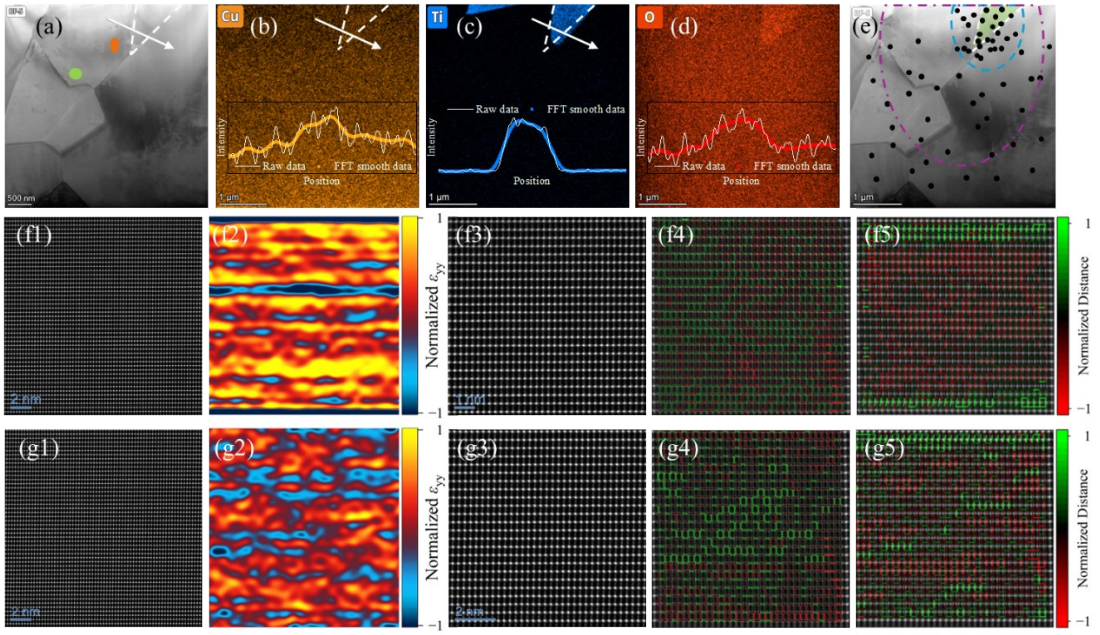

Figure S9 elucidate the effect of KT incorporation on the microstructure of KNN-based ceramics, using aberration-corrected transmission electron microscopy (AC-TEM). Figure S9 (a) displays the overall morphology of the analyzed region, with the KT-rich area outlined by dashed lines. Elemental mapping in Figures S9 (b-d) reveals a distinct

compositional difference between the KT region and the surrounding KNN grains, with a notably higher Cu content observed in the KT zone, additionally, the figure includes the element count intensity distribution curve corresponding to the white arrows, along with the results after FFT smoothing. Figure S9 (e) provides a schematic illustration of the resulting heterogeneous structure. Two regions were selected from Figure S9 (a) for detailed analysis. The corresponding HAADF-STEM images are shown in Figures S9 (f1) and (g1), while the calculated strain distribution of normalized ε_{yy} are given in Figures S9 (f2) and (g2) by using CalAtom software. These maps represent the deviation between the measured atomic positions and the average lattice reference, highlighting local strain fields induced by the presence of the KT phase. A single colorbar is shared by both maps, indicating the magnitude and sign of lattice distortion along the vertical direction. To further resolve local structural features, high-magnification images of the boxed areas are provided in Figures (f3) and (g3), the distributions of B-site and A-site interatomic distances for the region near the KT phase are shown in Figures S9 (f4) and (f5), respectively, while those for the region away from KT are presented in Figures S9 (g4) and (g5), respectively. A shared color scale is used to indicate the relative deviation of bond lengths from their mean values in either the horizontal or vertical direction. These quantitative maps reveal significant lattice distortion and bond length fluctuations near the KT-rich region compared to the KT-free matrix, particularly in the B-site framework.

Figure S10: (a) the hysteresis loops and (b) the bipolar strain curves of unpoled ceramics; (c) the hysteresis loops and (d) the bipolar strain curves of poled ceramics; (e) the unipolar strain curves of different KT doped; the internal bias field (E_i) and coercive field (E_C) of samples with different KT doping.

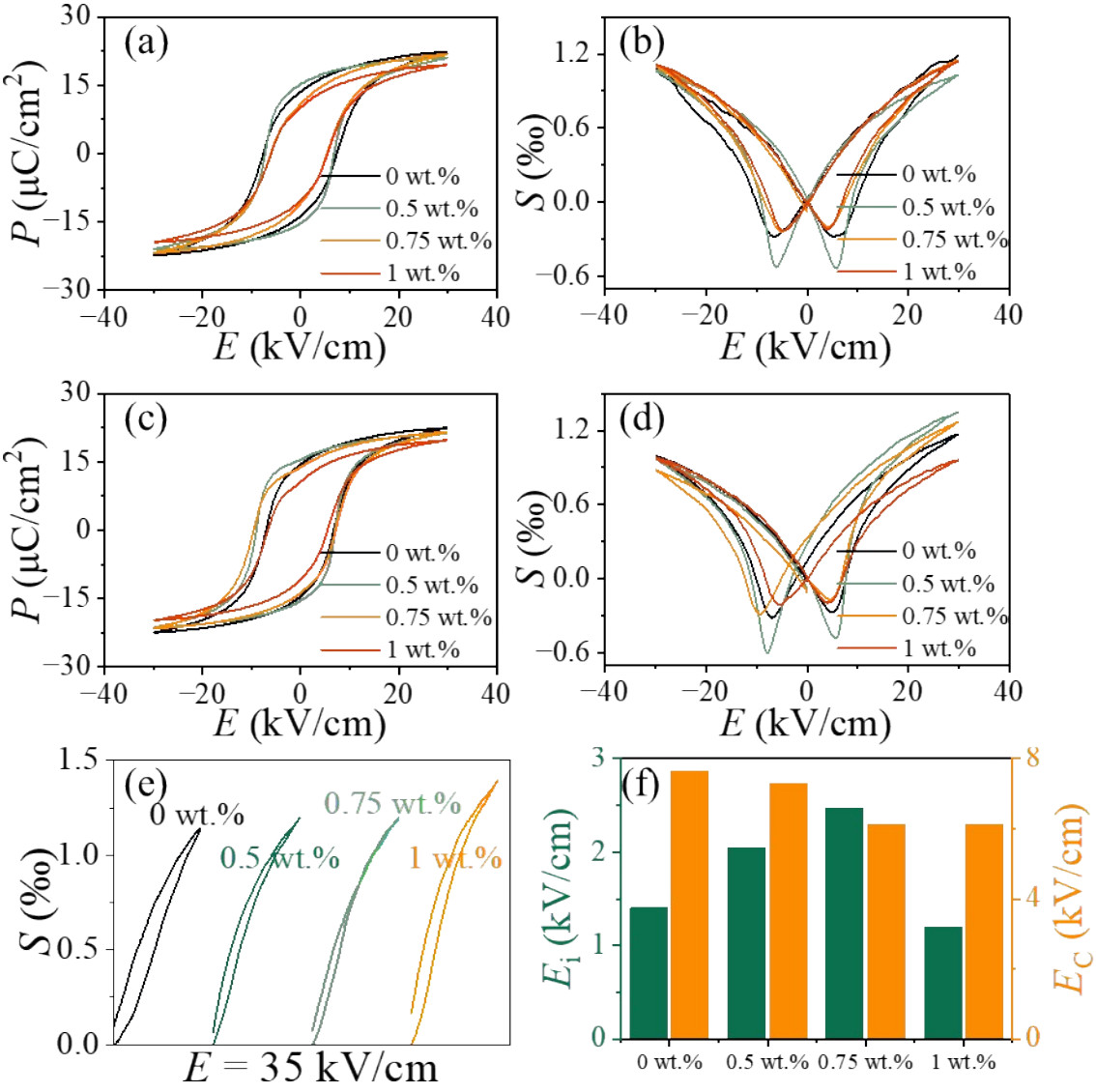

Figures S10 (a-b) compare the polarization hysteresis (*P*-*E*) and bipolar strain-electric field (*S*-*E*) responses of different KT-modified ceramics at 1 Hz under 30 kV/cm. (c) P-E loops and (d) S-E curves of poled samples; (e) unipolar strain curves; and (f) the evolution of E_i and E_C. Description for the unpoled samples (a-b), the maximum polarization (P_{max}) and positive strain (S_{pos}) remain relatively stable with increasing KT content, while the E_C exhibits a gradual decrease. The negative strain (S_{neg}) shows a non-monotonic trend, reaching its maximum at 0.5 wt.% KT. In contrast, the poled

samples (c-d) exhibit distinct asymmetry in their hysteresis loops due to the alignment of defect dipoles. As summarized in (f), the calculated E_i increases initially and peaks at 0.75 wt.% KT before declining. This maximum E_i at 0.75 wt.% indicates the strongest domain wall pinning effect at this composition, which correlates with the optimal mechanical quality factor (Q_m) observed in the main text. Moreover, unipolar strain behavior in Figure S10 (e) further highlights KT's dual role. As KT content increases, strain enhances and hysteresis narrows.

Figure S11: the normalized amplitude of (a1) 0 wt.% KT, (b1) 0.5 wt.% KT, (c1) 0.75 wt.% KT and (d1) 1 wt.% KT, and (a2-d2) shows the corresponding PFM phase images.

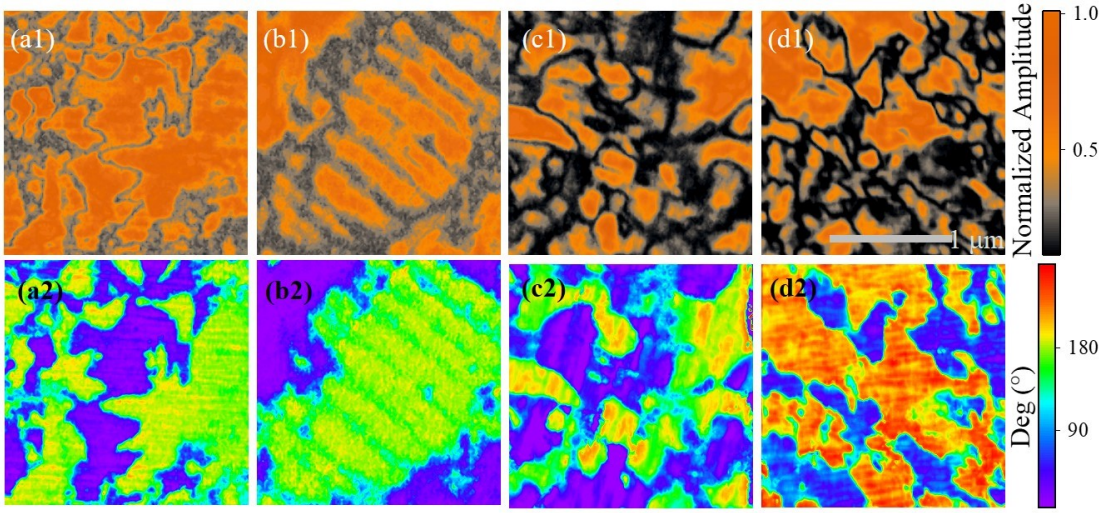

Figure S11 presents the PFM normalized amplitude and phase images of the ceramics with varying KT content. The phase contrast corresponds well with the amplitude signals, confirming the reliability of domain imaging. A clear trend that the initially large and well-defined domains in the 0 wt.% KT sample become increasingly fragmented and refined with the gradual incorporation of KT, reaching a markedly finer domain structure at 1 wt.% KT.

Figure S12: the strain as a function of (a) electric field and (b) stress field, simulated before and after the introduction of KT.

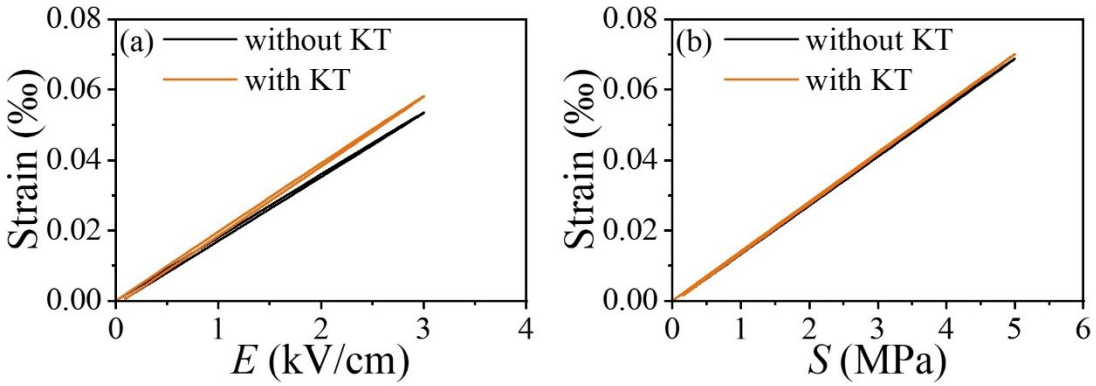

Figure S12 shows the simulated electric field-strain and stress-strain curves. The strain curves are derived by applying a small electric field and a low stress field along the [210] direction to the polarized domain structures obtained from phase-field simulations. The slope of the strain-electric field curve reflects the piezoelectric activity of the material, while the stress-strain curve is generated under a small cyclic mechanical load, and its hysteresis behavior is indicative of internal friction and mechanical energy dissipation. Specifically, to quantify the mechanical loss, we calculate the area enclosed by the stress-strain loop, which corresponds to the energy dissipated during one loading-unloading cycle (mechanical loss energy). The area under the loading curve represents the total input mechanical energy, while the difference between the input and recovered energy (from unloading) reflects energy loss. And the mechanical loss factor ($\tan(\delta_{mech})$) can be estimated as:

$$tan\delta_{mech} = W_{loss}/W_{stored}$$

where W_{loss} is the energy loss per cycle (loop area) and W_{stored} is the recoverable elastic energy. The strain of the samples is enhanced after the introduction of KT, indicating that there is an improvement in the piezoelectric activity of the samples, which is consistent with the fitting results in the main text section.